International Journal of Aeronautical & Space Sciences (2018) 19:363–374
https://doi.org/10.1007/s42405-018-0038-y

IJASS International Journal of Aeronautical and Space Sciences

ORIGINAL PAPER

Delamination Behavior of L-Shaped Laminated Composites

Tsinuel N. Geleta[1] · Kyeongsik Woo[2] · Bongho Lee[3]

Received: 4 January 2018 / Revised: 1 March 2018 / Accepted: 13 March 2018 / Published online: 12 May 2018

Abstract
We studied the delamination behavior of L-shaped laminated composites numerically and experimentally. In finite-element modeling, cohesive zone modeling was used to simulate the delamination of plies. Cohesive elements were inserted between bulk elements at each interlayer to represent the occurrence of multiple delaminations. The laminated composite models were subjected to several types of loading inducing opening and shearing types of delamination. Numerical results were compared to those in the literature and of experiments conducted in this study. The results were carefully examined to investigate diverse delamination initiation and propagation behaviors. The effect of varying presence and location of pre-crack was also studied.

Keywords Delamination · Curved laminate · Cohesive zone modeling · Multiple delamination

1 Introduction

Laminated composites are increasingly being used for a wide range of applications in industries such as aerospace, automotive, ship building, etc. Since one of the advantages of composite materials is monolithic construction, bends and curves are quite common in load bearing structural parts. One of these shapes is L-shaped laminates commonly formed, for example, at reinforcing ribs of hollow structures such as wings and wind turbine blades. The laminates may be formed from either unidirectional plies or from stacking of different types of textile composites.

When these L-shaped laminate structural parts are exposed to loads longitudinal and perpendicular to their legs, delamination occurs at the corner angular part. The delamination usually occurs due to development of inter-lamina tensile stress (ILNS) because of the curvature of the bend. In general, the resistance to delamination and other strength characteristics of the laminate is influenced by manufacturing quality, material properties, and geometric configurations. Issues related to the defect during manufacturing are actively studied by different researchers. For instance, Wijskamp et al. [1] studied shape distortions in composite forming of L-shaped laminates and other composite manufacturing. Ma et al. [2] proposed strategies to reduce the defects in the manufacture of contoured laminates. Other important manufacturing parameter studied by Brillant and Hubert [3] is thickness variation which was modeled and characterized for the case of L-shaped out-of-autoclave laminates.

As compared to ILNS, the effect of interlaminar shear stress (ILSS) on delamination has been relatively well studied [4–7]. The early works done on this topic such as Martin et al. [4,5] conducted a series of experiments and analytical work to predict delamination onset and growth in L-shaped laminates. Different methods of numerical analysis have also been applied to predict the delamination behavior of laminated L-shaped composites. Wimmer et al. [6,7] applied the Virtual Crack Closure Technique (VCCT) and the Linear Elastic Fracture Mechanics (LEFM) to predict the onset of interface damage and delamination progress. Another method employed by Gozluklu et al. [8,9] is the Cohesive Zone Modeling (CZM), where they considered mode mixities with initial crack. They used explicit dynamic finite-element analysis in conjunction with the CZM. In Ref. [8], the authors considered an initial crack placed at the middle of the curved part and mid-way between the plies. However, the determination of the location of the pre-crack was not clearly given. Moreover, the reference did not consider the occurrence of multiple delaminations between different plies. In Refs. [10,11], tests and finite-element analyses with CZM

✉ Kyeongsik Woo
kw3235@chungbuk.ac.kr

[1] Department of Civil and Environmental Engineering, Western University, London N6A-3K7, Canada

[2] School of Civil Engineering, Chungbuk National University, Chungbuk 28644, Republic of Korea

[3] Nextcoms Co., LTD, Daejeon 34037, Republic of Korea

were performed to study the delamination behavior of curved laminates. The predicted numerical results agreed well with those by tests. In these studies, multiple delaminations were considered and the effect of various cohesive properties and analysis parameters were discussed with an emphasis on the delamination initiation location.

We conducted analysis and experiment to investigate the delamination behavior of thick L-shape laminated composites. First, the configuration in Ref. [8] has been taken for the current study and was analyzed with and without an initial crack. The present results were compared to those of the reference for validation. Then, the configuration was extended to consider the possibility of multiple delaminations between different plies. Parametric study was also conducted on the location pre-crack by comparing it to the pristine case. Next, analysis and experiment were performed for a second configuration to further study the multiple delamination behavior of L-shape laminated composites. In numerical modeling, cohesive elements were inserted between laminae to simulate the initiation and propagation of delamination. The delamination behavior under opening and shearing load was systematically examined with a focus given on the occurrence of multiple delaminations at the curved part under opening load.

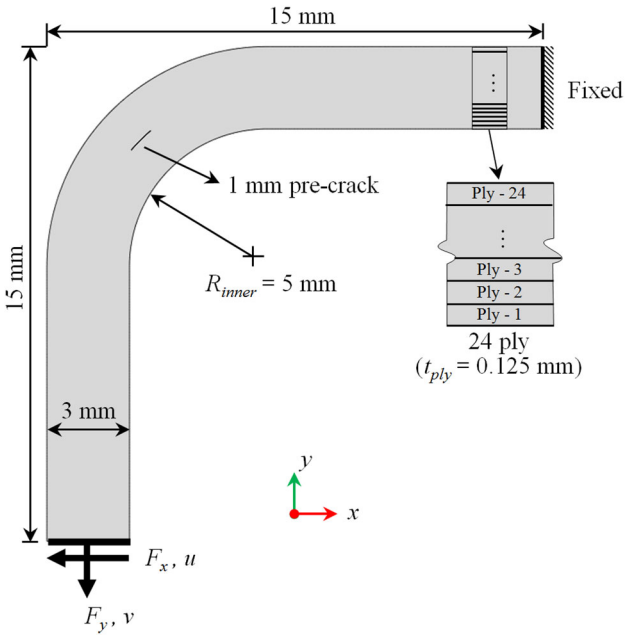

Fig. 1 Curved laminate configuration I (Config-I)

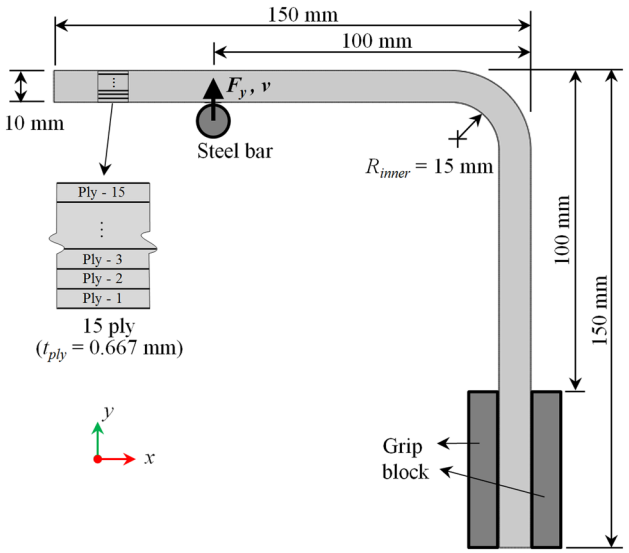

Fig. 2 Curved laminate configuration II (Config-II)

2 Analysis

2.1 Configurations

In this study, two configurations of L-shape curved laminates were considered. The first configuration (Config-I) shown in Fig. 1 was taken from Ref. [8], and was used for the validation of the present modeling and to study the delamination initiation and propagation behavior under various analysis conditions. The Config-I has equal two arms with each having 10 mm straight portions. The thickness and the width of the laminate were uniform 3 and 20 mm, respectively, and the inner radius at the bend was 5 mm. An initial crack of 1 mm length was placed at the middle of the curved part between plies 12 and 13 from a total of 24 plies. The location and presence of this pre-crack were later varied for the parametric study to determine the most critical location. The plies were unidirectional carbon/epoxy laminae. Each of the plies had 0.125 mm thickness. The plies are stacked and numbered, as shown in the figure, ply 1 being the bottom one on the horizontal arm. The top right edge of the L-shaped laminate is fully fixed as shown in Fig. 1. At the other edge, horizontal (F_x, u) and vertical (F_y, v) loads were applied alternatively.

The second configuration (Config-II) considered in this study is shown in Fig. 2 for which both the analysis and experiment were conducted. The Config-II has basically the same curved shape as the Config-I but with difference in material and dimensions. The laminate consisted of 15 tri-axially braided glass/epoxy composite plies. The curved part had the inner radius of 15 mm connected with two 135 mm straight arms. The thickness and the width of the *Config-II* were 10 and 50 mm, respectively. The laminate was fixed by 4 bolts at the lower right grip part and the vertical load was applied at the upper arm by a steel bar at 50 mm from the left end which produces opening deformation of the curved part.

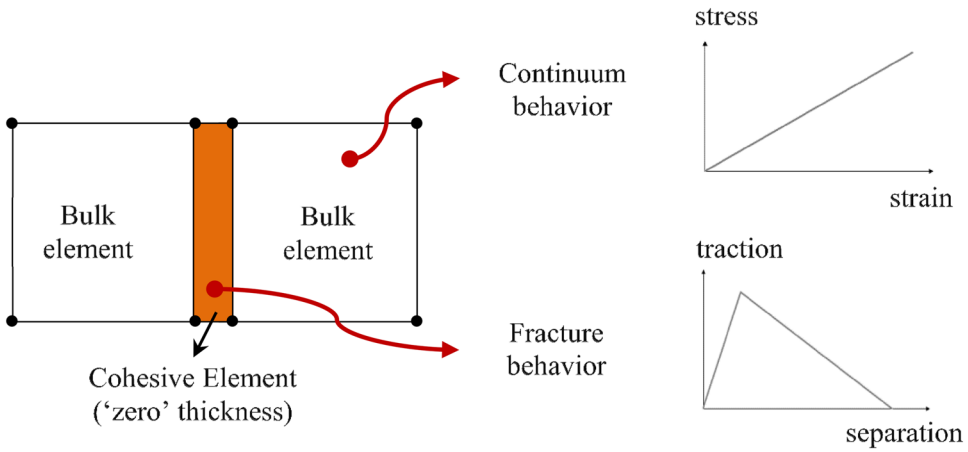

Fig. 3 Schematic insertion of cohesive element

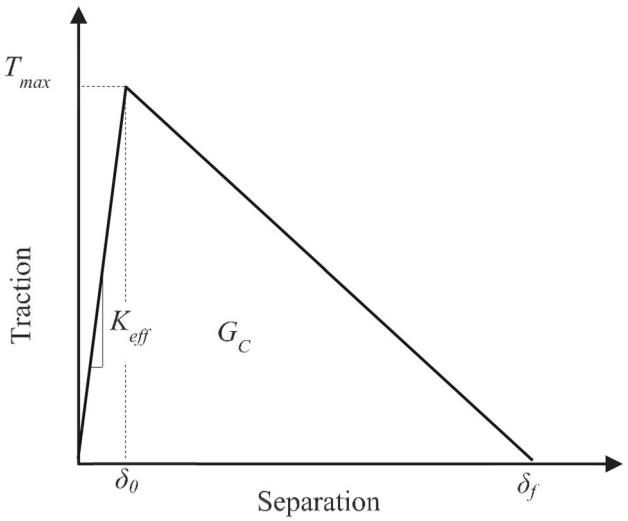

Fig. 4 Triangular traction-separation law

2.2 Cohesive Zone Modeling

Cohesive Zone Modeling (CZM) is a finite-element modeling technique in which crack propagation due to progressive separation of material interface can simulate damage of material. In CZM, special types of cohesive finite elements are used to simulate the discontinuity in the material. Dugdale [12] and Barenblatt [13] are among the pioneers who suggested the cohesive zone model to simulate the failure characteristics of brittle materials. The finite-element CZM analysis was first applied by Hillerborg et al. [14] to cracking in a concrete beam under bending. Later on, further advances were made by a number of researchers and successfully applied to study the linear elastic and elasto-plastic crack propagation of engineering materials (eg., [15–26]), as well as composite delamination problems (eg., [27–31]]).

Modeling of material discontinuity using CZM involves the insertion of 'zero' thickness cohesive elements between the regular bulk finite elements, as shown in Fig. 3. These cohesive elements are inserted at locations, where delamination is suspected to happen. The behavior of the bulk elements is the usual elasto-plastic manner under all loading levels. However, the cohesive elements between the bulk elements have a special behavior defined by a specified traction-separation law (TSL) [17]. These 'zero' thickness cohesive elements represent discontinuity in structure by acquiring a finite volume when the conditions set by the TSL is satisfied. Once they deform beyond their limit of TSL, the elements do not transfer any force, which is essentially equivalent to void space. Several models of TSLs have been proposed by different researchers over the years, which have been reviewed in Ref. [17], including exponential [16], cubic polynomial [18], trapezoidal [15], triangular [18], linear and polynomial softening [20–22], and hardening–softening [23–26].

In this study, the triangular TSL was used. As shown in Fig. 4, this TSL is defined by the maximum traction (T_{max}), cohesive stiffness (K_{eff}), initial failure separation (δ_0), final failure separation (δ_f), and fracture energy (G_c). The maximum traction is the amount of traction carried by the cohesive element before fracture initiates. The initial slope of the triangular TSL is the effective cohesive stiffness (K_{eff}). The fracture energy, which is the area under the curve, is defined as the consumed energy through the creation of new fracture surface. The initial and final failure displacements or separation limits are the values that determine the onset and propagation of fracture, respectively.

The values of these parameters are obtained in different ways. The fracture energy is a material property determined by experiments. For composite delamination, it can be measured from experiments like the Double Cantilever Beam (DCB) [27], End Notched Flexure (ENF) [28], and Mixed Mode Bending (MMB) [29]. The maximum interface traction was observed to have some influence in the predicted results as studied by Refs. [30–32]. Ref. [31] studied the effect of $T_{\max}$ on the accuracy of the results and on the convergence behavior which is also dependent on the mesh size and

Table 1 Elastic properties

	E_{11} (GPa)	E_{22} (GPa)	E_{33} (GPa)	ν_{12}	ν_{13}	ν_{23}	G_{12} (GPa)	G_{13} (GPa)	G_{23} (GPa)
Config-I	138	10	10	0.3	0.3	0.27	5.24	5.24	3.93
Config-II	33	2.5	20	0.3	0.3	0.3	2.2	5	2

Table 2 Cohesive properties

	K (MPa)	T_1 (MPa)	T_2 (GPa)	G_{IC} (N/mm)	G_{IIC} (N/mm)	η (B-K)
Config-I	$10^3 \times E_{22}$	60	80	0.352	1.002	1.75
Config-II	$10^3 \times E_{22}$	15	77	0.6	1.25	1.8

Table 3 Constituent properties for Config-II

	Name	Used for	E (GPa)	Strength (MPa)	Elongation (%)
Fiber	TR50S-12L	Axial tow	240	4900	2.0
	37-800WD	Bias tow	255	5490	2.2
Matrix			2.904	74.3	4.97

other parameters which are discussed further below. Another important parameter to be determined is the cohesive stiffness for which different guidelines have been given by different authors. In Ref. [31], it was shown that the cohesive stiffness may have significant effect resulting in much softer elastic response known as added compliance effect if either the number of cohesive elements is large or they have finite thickness. Since the cohesive elements are needed to simulate the fracture only, their effect on the compliance should be minimized. The value of K_{eff} becomes especially important when the number of cohesive elements inserted in the model is large and when cohesive elements are inserted in multiple layers. To minimize the added compliance, K_{eff} should be kept as large as possible as compared to the bulk element stiffness [31]. However, too large, a value may increase numerical error and create problems in solution convergence. In this study, a series preliminary analyses were performed and the cohesive stiffness value was selected that produced less than 0.5% difference in the elastic response compared to the bulk element-only model.

2.3 Material Properties

The material properties required to conduct CZM analyses are divided into two. The first is the continuum properties of the material in damage-free regions, while the other is the de-cohesion properties of the material near crack initiation and propagation. As briefly discussed before, the modeling technique involves two types of elements. The first is the bulk finite elements that behave in elastic manner. The other types are the cohesive elements whose properties are defined by the type of TSL adopted in the model.

Tables 1 and 2 summarize the elastic and cohesive properties used in the current paper. Here, subscripts 1 and 2 indicate the major in-plane and out-of-plane directions, respectively, while subscript 3 indicates the minor in-plane direction. For the Config-I, the laminate was made by stacking T300/977-2 carbon/epoxy laminae. Since it was adopted from Ref. [8], the elastic and cohesive properties were also taken from the same.

For the Config-II, the lamina material was triaxially braided carbon/epoxy composite with two types of carbon fibers of TR50S-12L and 37-800WD [32]. The constituent fiber and matrix properties are given in Table 3. The overall fiber volume fraction (v_{fT}) of the triaxially braided lamina was measured to be 47.38%. The effective properties for triaxial braid lamina were obtained using multi-scale analyses: micro- and meso-mechanics. Herein, a brief description is given. (The detailed process is found in Ref. [33].) First, the effective properties of axial and bias tows were calculated micromechanically, since the tows consisted of fiber and matrix. In this case, several approaches can be used including rule of mixtures [34], SME [35], finite-element unit-cell analysis, etc. In this study, a commercial software GENOA/MCQ [36] was used to obtain the tow properties. Next, a finite-element meso-scale unit cell analyses were performed to obtain the effective properties of triaxially braided composite. For this, the unit cell of triaxially braided composite was modeled, as shown in Fig. 5, using the measured dimensions of axial and bias tows. Since the tow path of the bias tows continuously changes, material directions were defined for proper material property transformations. Finally, the effective properties given in Table 1 were obtained from a series of analyses simulating uniaxial and shear tests in each direction.

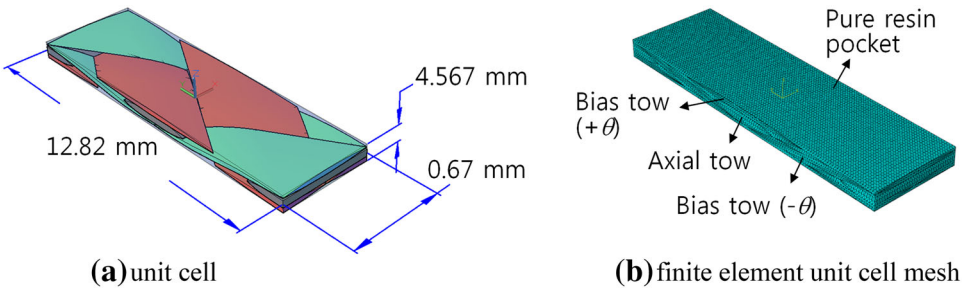

(a) unit cell **(b)** finite element unit cell mesh

Fig. 5 Meso-scale unit cell modeling of triaxially braided composite **a** unit cell **b** finite-element unit cell mesh

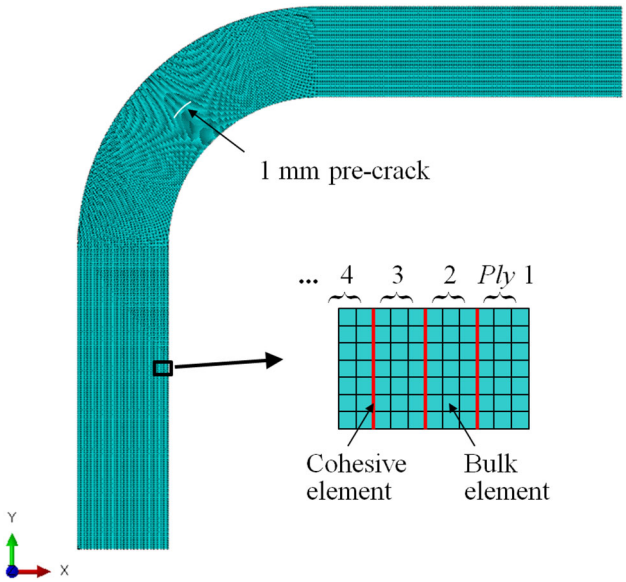

Fig. 6 FE mesh for Config-I

For the cohesive properties of Config-II, currently, no standard test method exists to measure the interlaminar fracture properties of textile composites. While the fracture properties textile composites can be obtained by applying test methods for unidirectional composites (eg., Refs. [37,38]), in this study, the values of interlaminar fracture energy and maximum traction of Config-II were determined instead from a series of preliminary analyses as the ones that matched the experimental load–displacement curves. For Config-II, the initiation and growth of the first delamination were mainly in mode I. Thus, the maximum traction and fracture energy of mode I were determined to be the ones that produced the matched value of the peak load and the following load–displacement curve of the test. Cohesive properties of mode II were similarly determined.

2.4 FE Modeling

The finite-element modeling of the L-shape curved laminate was made by separately modeling every ply and joining them with zero thickness cohesive elements. Four node plane strain elements were used as bulk elements with every ply having three elements across the thickness.

In CZM, the size of cohesive elements near the fracture region is an important aspect for the accuracy and convergence of the analysis. The cohesive zone is defined as the region within cohesive zone size (l_{cz}) distance from the crack tip. This distance is the distance from the crack tip to the point where the maximum cohesive traction is attained. As given by Turon et al. [31], the cohesive zone size is expressed as

$$l_{cz} = M\frac{EG_c}{\left(\tau^0\right)^2} \tag{1}$$

where E is the Young's modulus, G_c is the fracture toughness, τ^0 is the maximum interfacial traction, and M is a parameter that depends on each cohesive zone model. One of the widely applied cohesive zone models is that of Hillerborg et al. [14] in which the value of M is approximately one, which was adopted in this study also.

Once l_{cz} is estimated, the cohesive element size (h^e) can be determined. If the number of cohesive elements in l_{cz} is N^e, then the following relation can be used for the determination of the element size:

$$h^e = \frac{l_{cz}}{N^e}. \tag{2}$$

Different suggestions were made for the minimum number of elements to be included in the cohesive zone. This number is important to decide the optimal size of elements between accuracy of analysis and computational efficiency. Moes and Belytschko [39] recommended the use of more than ten elements in the zone, while Davila et al. [40] suggested that using three elements would be sufficient. Other suggestions were also summarized by Turon et al. [31].

Based on the properties given in Tables 1 and 2, the cohesive zone sizes for the Config-I and Config-II were calculated from Eq. (1) to be 0.987 and 6.7 mm, respectively. In this study, the sizes of the cohesive elements (and thus the size of bulk elements) in the direction of crack propagation were determined so that at least ten elements in the cohesive process zone following the recommendation of Ref. [39].

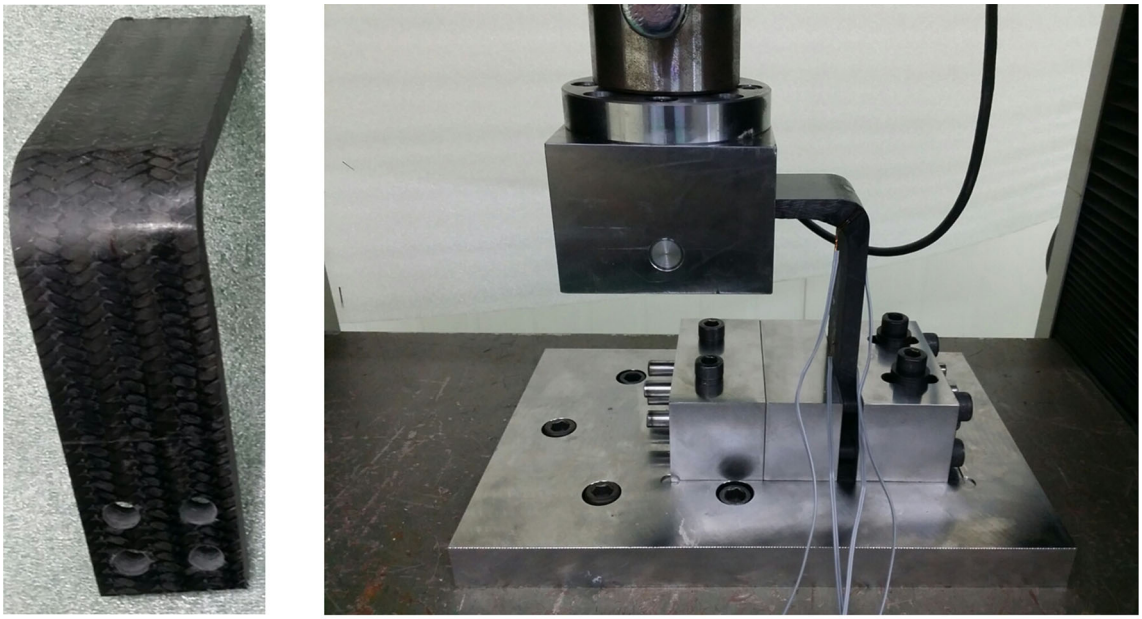

Fig. 7 Specimen preparation and test setup. **a** specimen, **b** test setup

In the present study, the analysis was performed using Abaqus. Figure 6 shows the mesh for the Config-I. This mesh consisted of 22,392 plane strain bulk elements and 7153 cohesive elements. Three elements per ply were used in the thickness direction for accurate simulation. Cohesive elements were inserted to the pre-generated bulk element mesh using in-house. Surface-to-surface contacts were defined to avoid penetration of delaminated plies after delamination in multiple interlayers. The mesh for the Config-II was generated similarly using 13,770 bulk elements and 4284 cohesive elements for the laminate part. Additional 262 bulk elements were used to model the steel bar. Surface-to-surface contact was defined between the steel bar and the laminate to allow the load applied to the steel bar was transformed to the laminate. For both configurations, general static analyses were performed by applying displacement loads in the desired direction.

The quadratic stress criterion (QUADS) was used for failure initiation. For failure evolution, energy-based criterion was used with BK law [29] for the mixed mode behavior. It should be noted that, in the preliminary analyses, a very abrupt delamination initiation and propagation was found within a very short increase of applied load. This pattern repeated as multiple delaminations occurred at various locations in different layers in different load levels. To capture accurately the delamination initiation points as well as correct delamination mode, the analysis was divided into several steps and the load increment was carefully controlled.

3 Experiment

Delamination tests were performed for the laminate of the Config-II. The detailed specimen dimensions, grip, and loading scheme are shown in Fig. 2. Test specimens were manufactured by vacuum assistant resin transfer method (VARTM). Triaxially braided preform mats were placed on L-shape mold, bagged with release fabric, flow medium and vacuum film, injected resin, and cured at the designated temperature. Then, the cured curved laminate was cut to specified dimensions and four bolt holes were made by machining at the grip part, as shown in Fig. 7a.

Figure 7b shows the test setup. The lower end of the specimen was fixed to steel grip block by four bolts and the load was applied at 50 mm from the edge of the upper arm by steel bar. The load applying cross-head speed was 2 mm/min. The history of load and cross-head displacement was recorded. The delamination propagation image at one side of the specimen was also recorded by high resolution camera.

4 Results and Discussion

In this section, numerical and experimental results are discussed. First, the delamination of the L-shaped laminate of Config-I with a pre-crack was analyzed under vertical loading that caused the delamination propagating in shear mode. The result compared to that in Ref. [8] for model verification. Then, parametric studies were conducted on Config-I by varying the loading direction and pre-crack conditions in

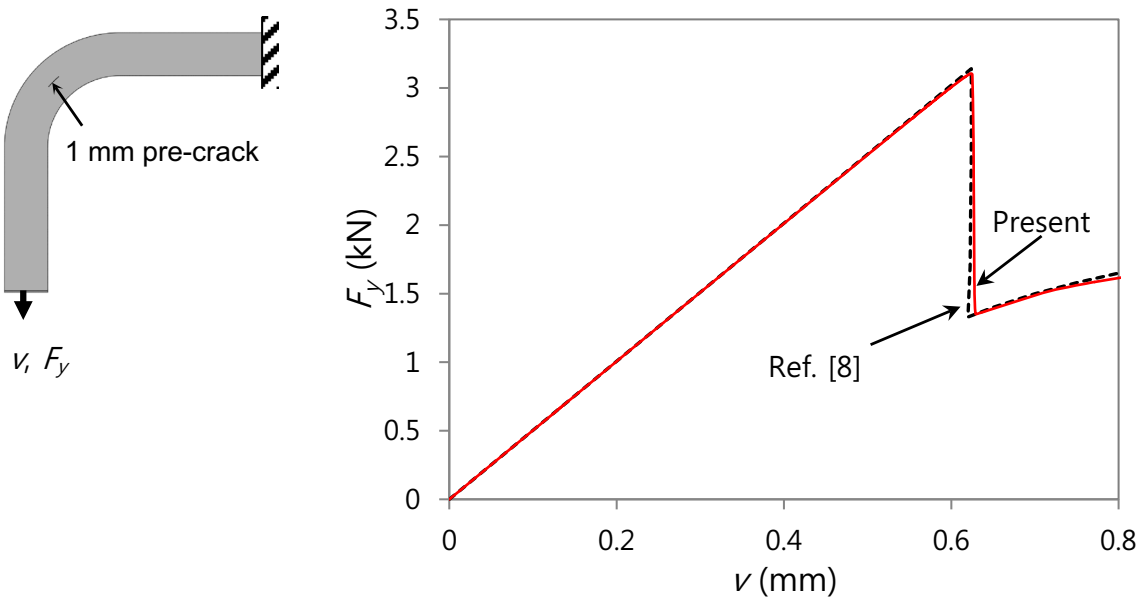

Fig. 8 Load–displacement curve for Config-I under vertical loading

each loading direction. Next, the analytical and experimental delamination results of Config-II were examined. Comparisons of different cases are also given.

4.1 Delamination Behavior of Config-I

Figure 8 shows the load–displacement curves for Config-I subjected to a vertical loading applied at the lower edge. In this case, a pre-crack of 1 mm length was located at the mid-interface of the center of the curved region. As seen in the figure, the numerical result matched excellently to that of Ref. [8] validating the present finite-element modeling. In the figure, the load increased, reached its peak value, dropped abruptly, and then started to increase again. The load drop occurred within a very short increment of displacement and corresponded to the point when the delamination initiated and propagated at the tips of the pre-crack. Once started, the delamination propagated very fast in the curved region. However, as the delamination approached the boundary of the curved-straight region. The propagation speed slowed down quite a bit and a slow-steady propagation followed in the straight region, which corresponded to the slow increase of the load after the sudden drop.

In Fig. 8, the pre-crack was placed at the mid-interface of the center of the curved region. However, this location was found not to be the primary candidate of delamination initiation location. Figure 9 shows the delamination initiation and propagation history for the same configuration without pre-crack. Delamination propagation history can be seen from the shear stress distribution, since this stress is the main cause for delamination in the case of vertical loading. The delamination started at the mid-plane between plies 12 and 13 of the upper arm part at approximately 7.4 mm away from the right end. Once generated, the delamination propagated very quickly in both directions, resulting in the significant load decrease. After the delamination propagated past the curved part and reached the starting point of the lower straight arm part, the delamination growth slowed down again and had the slow-steady propagation afterwards.

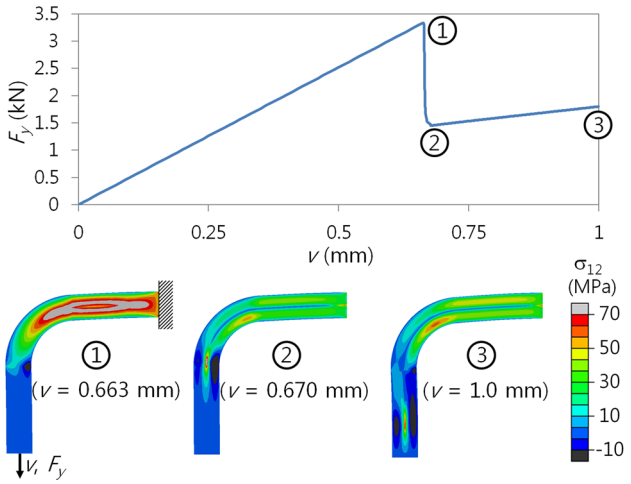

Fig. 9 Delamination propagation history for vertical loading without pre-crack

The effect of pre-crack location was assessed under the vertical loading. In Fig. 10, three load–displacement curves were compared. The first is the case where there is no pre-crack (Fig. 9), the second is where the pre-crack is located mid-way along the curved part (Fig. 8), and the third is where

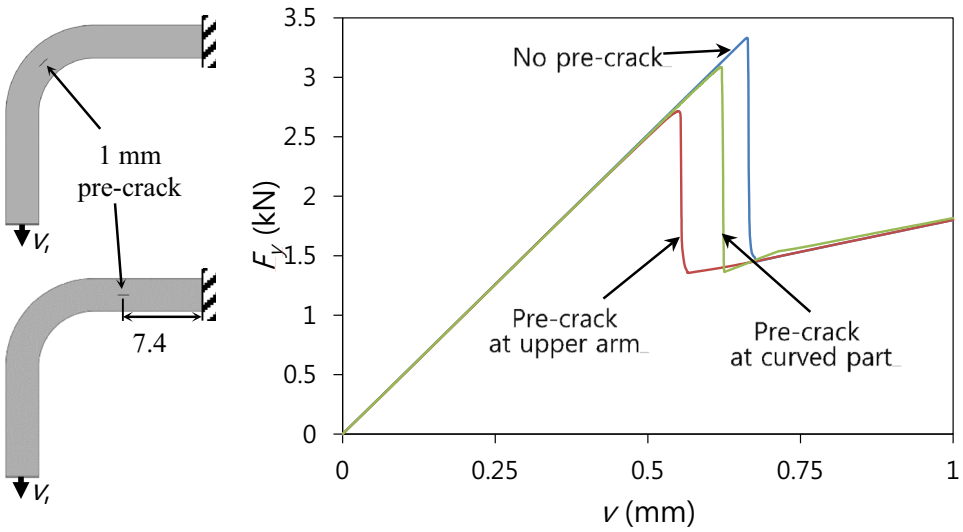

Fig. 10 Effect of pre-crack under vertical loading

the pre-crack is located at the upper arm 7.4 mm away from the right end. (This was the corresponding delamination initiation location for no pre-crack case.) Comparing the results, the case where the pre-crack was located at the upper arm showed the smallest peak load. The case with no pre-crack has reasonably higher peak load from the three. The relative reduction of the peak load compared to the one without pre-crack was 7.2 and 17.0% when the pre-crack was located at the mid-way of the curved part and at the upper arm, respectively, which indicated that the existence and location of the pre-crack had an important effect resulting in marked reduction in the strength of the L-shape composite laminates.

Similarly, the delamination behavior of Config-I was also studied under horizontal loading or opening loading. (This loading opens the curved part.) A horizontal displacement was applied at the lower edge in the negative direction to have an opening deformation of the curved part. Figure 11 shows the load–displacement for the case without pre-crack. In this case, the displacement was continuously applied to allow multiple interface delaminations occurring in various locations. The first delamination occurred at a larger displacement magnitude than that for the vertical loading case. It occurred between plies 10 and 11 at approximately $\theta = 22.5^{\circ}$ from the upper end of the curved part. In Fig. 11, the circled numbers correspond to the deformed shapes of the laminate at the specific level of loading, and indicate major milestone points in delamination propagation history. A delamination corresponded to a sudden drop in the load–displacement curve and then the supported load again increased until the next delamination. In the figure, the load drop corresponding to this delamination is the part of the load–displacement curve from points 1 to 2. The first delamination propagated up to both ends of the arms before the second delamination started. After the first delamination, the curve increased up to point 3, where the second delamination occurred between plies 16 and 17, also at the upper end of the curved part. Unlike the first one, this delamination propagated to the end of the upper arm only. Then, the third delamination occurred between plies 4 and 5 followed by several delaminations at different locations.

Comparing the two loading directions, some differences can be observed. First, the horizontal loading case has failure load one third of the vertical loading case. It attained this smaller failure load at larger displacement than the vertical loading case. This means, the L-laminate is more flexible but weaker when it is loaded horizontally. The second observation is that in the horizontal loading case crack initiated in the curved part, while it started in the upper arm for the case of the vertical loading.

The pre-crack was also found to affect the delamination behavior under horizontal loading. As shown in Fig. 12, the existence of pre-crack greatly diminished the peak load value under the horizontal load. Here, the 1-mm pre-crack was located at $\theta = 22.5^{\circ}$ and between plies 10 and 11 ($r = 6.25$ mm), at $\theta = 22.5^{\circ}$ and between plies 12 and 13 ($r = 6.5$ mm, mid-plane), and at $\theta = 45^{\circ}$ and between plies 12 and 13 ($r = 6.5$ mm, mid-plane). The figure shows that all cases with pre-crack had significant first peak load reductions ranging between 35.1 and 41.2% compared to that without pre-crack. It was found that, after the first delamination, the cases with no pre-crack and with pre-crack between plies 10 and 11 showed almost identical load–displacement curves. This behavior was also observed for the cases, where the pre-crack was placed between plies 12 and 13. In addition, similar delamination shapes at the applied displacement $u = 5$ mm, although now shown here, were obtained for group of cases that had the same interface location of the first delamination or the pre-crack, indicating that the load–displacement curves and the delamination pattern were dependent on the location of the first delamination.

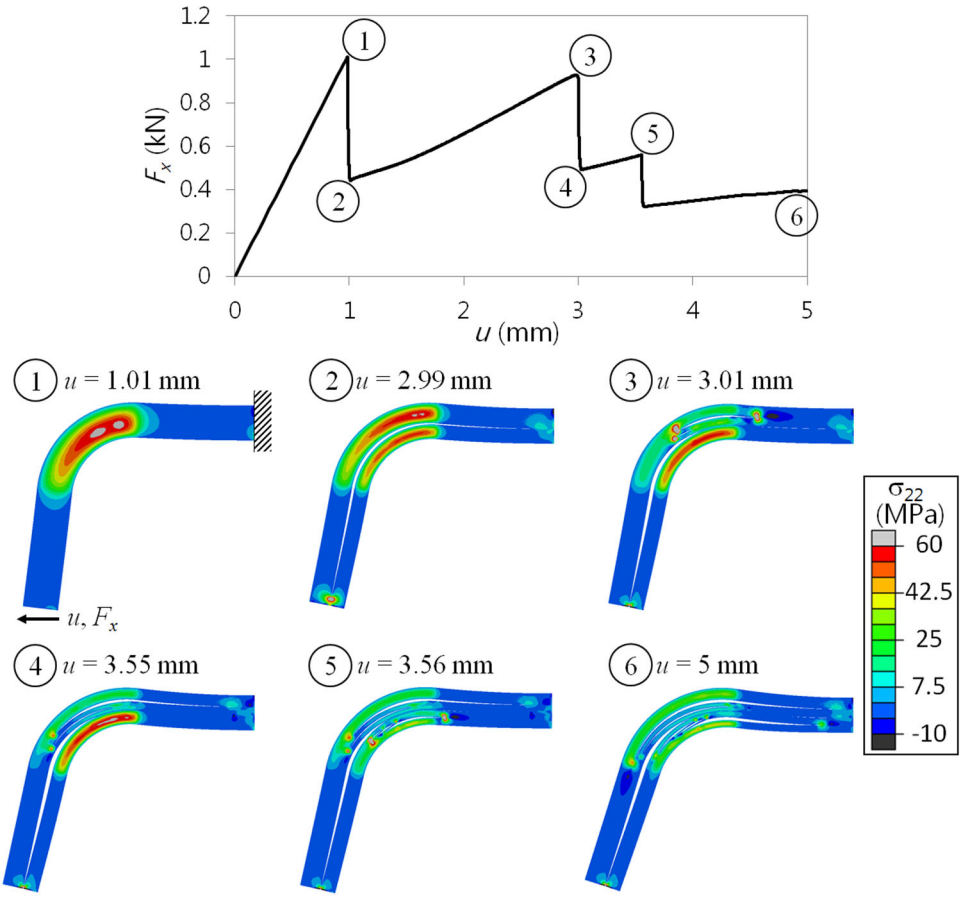

Fig. 11 Delamination propagation history for horizontal loading without pre-crack (displacement scale factor = 1)

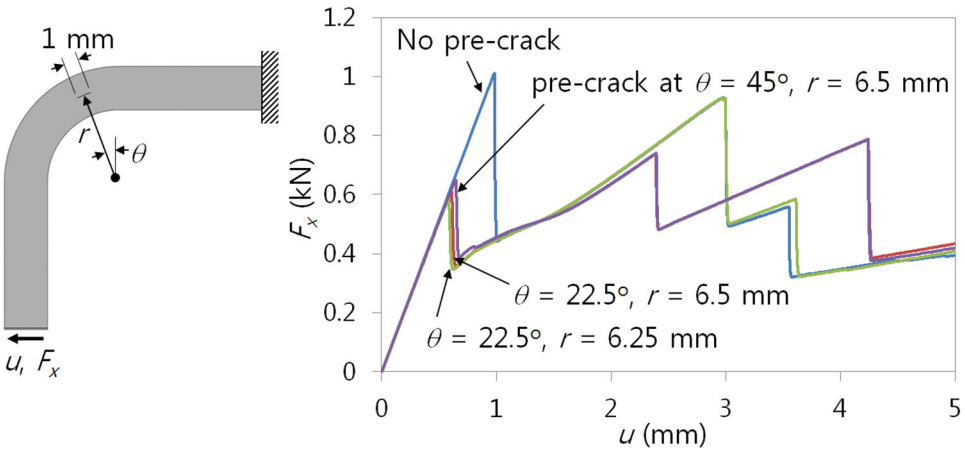

Fig. 12 Effect of pre-crack on load–displacement curve under horizontal loading

4.2 Delamination Behavior of Config-II

The delamination behavior of Config-II was studied both numerically and experimentally. Figure 13 compares the load–displacement curves obtained from experiment and analysis. The comparison between test and analysis results is given in Table 4. As can be seen in both the figure and the table, the two curves matched reasonably well in the first half portion of the graph when the applied displacement (v) was between 0 and 14 mm, correctly predicting the first and the second major drops. However, they did not beyond when$v$ was larger than 15 mm. As discussed below, when v was less than 14 mm, there occurred four delaminations with only one propagating through the curved part. Thereafter, however, many delaminations developed and grew simultaneously interacting with one another. The complicated interaction of the many delaminations in the diverse locations and different ply interfaces was not able to be accounted for accurately with the present modeling. In addition, two-dimensional assumption in the width direction

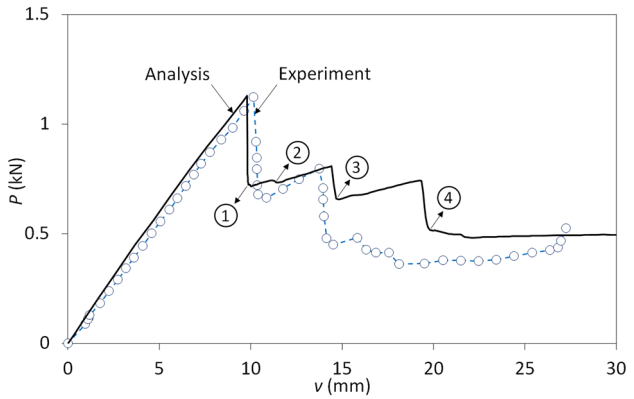

Fig. 13 Experimental and analytical load–displacement curves for Config-II

Table 4 Comparison of peak loads and corresponding displacements for Config-II

	P (N)			*v* (mm)		
	Test	Analysis	Diff. (%)	Test	Analysis	Diff. (%)
1st peak	1123	1130	0.62	10.15	9.80	3.44
2nd peak	797	809	1.50	13.75	14.43	4.95

and the random distribution of geometric and material property variation could be factors which were not considered herein. These were thought to result in the mismatch in the latter half part.

In Fig. 13, the circled numbers indicate a part of major milestones of the delamination initiation and propagation history, for which deformed shapes are plotted in Fig. 14. The first delamination initiated at the interface between plies 6 and 7 (out of total 15 plies) and approximately 30° from the lower end of the curved part when v was 9.8 mm. It propagated quickly through the curved part in both directions and caused a significant drop in the load (point 1). The second delamination occurred when v was 11.66 mm at the lower arm-curved part transition region between plies 7 and 8 (point 2), and the third delamination followed right after at the upper arm-curved part transition region between plies 6 and 7. However, these delaminations propagated only in the transition region and did not propagated through the mid-way of the curved part, causing only small load drops. The fourth delamination occurred at the upper transition region between plies 8 and 9, which did not cause a notable load drop either. The fifth delamination occurred when v was 14.6 mm at the mid-way part of the curved region between plies 3 and 4 (point 3). The fifth delamination caused the second significant load drop; however, the size of the load drop was smaller and the slope was less stiff compared to those of the first delamination. This was because the amount of elastic energy released at the first delamination was much larger than that of the fifth delamination. In addition, while only one delamination growth constituted the energy release at the time of the first delamination, the energy was released by 5 delamination growths, resulting in much less stiff load-drop curve. When v was increased further, several new delaminations initiated and grew near the end region of the curved part, not showing notable decrease in the load, until the eighth delamination developed at the mid-way of the curved part between plies 12 and 13 (point 4).

Figure 15 compares the delamination shape when $v = 25$ mm. In the experimental image, delaminations were marked by red lines to help viewing. The general delamination pattern obtained from the experiment and analysis matched reasonable well. Although the shapes did not match exactly, the predicted delamination shape was thought to be acceptable considering the complicated interaction during growth between delaminations as discussed previously. Both results showed that multiple delaminations developed in various interfaces, and that the delaminations mainly initiated and propagated in and near the curved part.

The delamination pattern of the Config-II was different from that of the Config-I under opening load. For the Config-I, multiple delaminations occurred too but some propagated through the curved part and the straight arm parts reaching to the end of the specimen. In addition, contact occurred between some of the sub-laminates after delamination. In contrast, the delamination developed in and near the curved part and did not propagate to the grip or the loading point in Config-II. No contact between separated sub-laminates was observed, either. This difference was thought to be related to the difference of mode mixity resulting from the difference of moment–shear ratios, as well as the difference in fracture properties. Under the opening load, the delamination initiated near the mid-way of the curved part was predominantly in the opening mode (mode I), but when it propagated to the straight arm parts, it became an opening–shearing (mode I–mode II) mixed mode crack. Since the maximum traction and fracture energy values of mode I are smaller than those of mode II, the delamination initiates and propagates relatively easily near the mid-way region of the curved part, while these are less easy in the straight arm parts. (This explains the slowing down of the delamination propagation near the curved-straight boundary region.) Between the two configurations, the Config-II had the larger moment to shear force ratio at the curved part than the Config-I due to the longer arm length to thickness ratio. As a result, the delamination mode of the Config-II was more in opening than in shearing compared with that of Config-I, and thus tended to have the delamination development concentrated in the curved part.

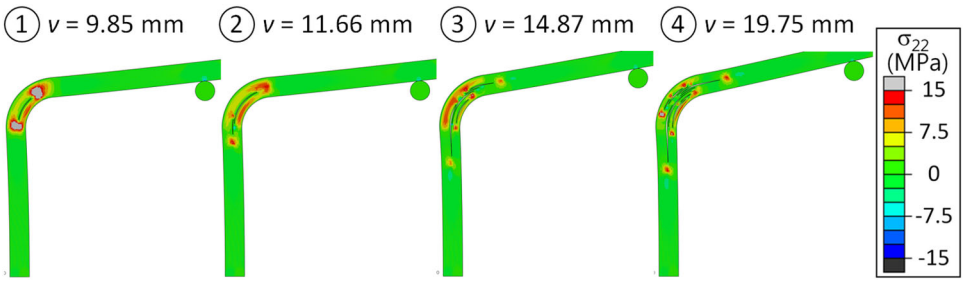

Fig. 14 History of delamination initiation and propagation for Config-II

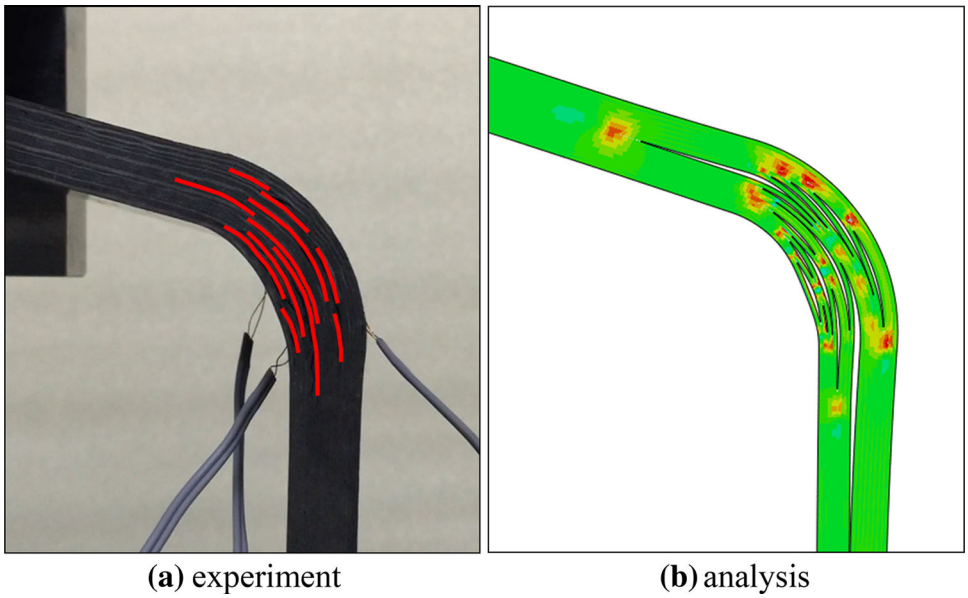

Fig. 15 Comparison of experimental and analytical delamination shapes of Config-II **a** experiment, **b** analysis

5 Conclusion

The delamination behavior of L-shaped laminated composites was studied using cohesive zone modeling. Two configurations were considered: one taken from a reference against which the numerical result was validated (Config-I), and one for which both experiment and analyses were performed (Config-II). In the finite-element modeling, first bulk element mesh was generated and then cohesive elements were inserted between all ply interfaces. The predicted load–displacement curve matched accurately to that in the reference for Config-I and to that by experiment for Config-II, which validated the present numerical modeling.

It was found from parametric studies for Config-I that generally the horizontally loaded case had lower failure strength and higher failure displacement as compared to the vertical loading one. For pristine model, the delamination initiation occurred at the mid interlayer of the upper arm under vertical loading, while it occurred at 22.5° location of the inner interlayer under horizontal loading. For both loading cases, the maximum loads were significantly dependent on the existence and the location of pre-crack. Between Config-I and Config-II under opening load, different delamination propagation pattern was obtained due to different loading arm lengths. Most delaminations developed and stayed in the curved part for the latter configuration with a longer arm length, while many propagated well out of the curved part for the former one with shorter loading arm.

Acknowledgements This work was supported by Defense Acquisition Program of Korea through Dual Use Technology Development Project 2016.

References

1. Wijskamp S (2005) Shape distortions in composites forming. University of Twente, Enschede
2. Ma Y, Centea T, Nutt SR (2017) Defect reduction strategies for the manufacture of contoured laminates using vacuum BAG-only prepregs. Polym Compos 38(9):2016–2025
3. Brillant M, Hubert P (2011) Modelling and characterization of thickness variations in L-shape out-of-autoclave laminates. In: 18th Int. Conf. Compos. Mater
4. Martin RH, Jackson WC (1993) Damage prediction in cross-plied curved composite laminates. In: Stinchcomb WW, Ashbaugh WC (eds) Composite materials: fatigue and fracture, vol 4. ASTM STP 1156. ASTM, Philadelphia, pp 105–126
5. Martin RH (1992) Delamination failure in a unidirectional curved composite laminate. In: Grimes GC (ed) Composite materials testing and design, vol 10. ASTM STP 1120. American society for testing and materials, Philadelphia, pp 365–382

6. Wimmer G, Pettermann HE (2008) A semi-analytical model for the simulation of delamination in laminated composites. Compos Sci Technol 68:2332–2339
7. Wimmer G et al (2009) Computational and experimental investigation of delamination in L-shaped laminated composite components. Eng Fract Mech 76:2810–2820
8. Gözlüklü B, Coker D (2012) Modeling of the dynamic delamination of L-shaped unidirectional laminated composites. Compos Struct 94:1430–1442
9. Gözlüklü B, Uyar I, Coker D (2015) Intersonic delamination in curved thick composite laminates under quasi-static loading. Mech Mater 80:163–182
10. Nguyen KH, Ju HW, Truong VH, Kweon JH (2018) Delamination analysis of multi-angle composite curved beams using an out-of-autoclave materials. Compos Struct 183:320–330
11. Truong VH, Nguyen KH, Park SS, Kweon JH (2018) Failure load analysis of C-shaped composite beams using a cohesive zone model. Compos Struct 184:581–590
12. Dugdale DS (1960) Yielding of steel sheets containing slits. J Mech Phys Solids 8(2):100–104
13. Barenblatt GI (1962) The mathematical theory of equilibrium cracks in brittle fracture. Adv Appl Mech 7:55–129
14. Hillerborg A, Modéer M, Petersson P-E (1976) Analysis of crack formation and crack growth in concrete by means of fracture mechanics and finite elements. Cem Concr Res 6:773–782
15. Tvergaard V, Hutchinson JW (1992) The relation between crack growth resistance and fracture process parameters in elastic-plastic solids. J Mech Phys Solids 40(6):1377–1397
16. Xu X-P, Needleman A (1994) Numerical simulations of fast crack growth in brittle solids. J Mech Phys Solids 42(9):1397–1434
17. Park K, Paulino GH (2013) Cohesive zone models: a critical review of traction-separation relationships across fracture surfaces. Appl Mech Rev 64(6):060802 (20 pages)
18. Tvergaard V (1990) Fibre debonding and breakage in a whisker-reinforced metal. Mater Sci Eng A 125(2):203–213
19. Camacho T, Ortiz M (1996) Computational modelling of impact damage in brittle materials. Int J Solids Struct 33(20–22):2899–2938
20. Petersson PE (1981) Crack growth and development of fracture zones in plain concrete and similar materials. Lund Institute of Technology, Lund
21. Wittmann FH et al (1988) Fracture energy and strain softening of concrete as determined by means of compact tension specimens. Mater Struct Constr 21:21–32
22. Sills R, Thouless MD (2013) The effect of cohesive-law parameters on mixed-mode fracture. Eng Fract Mech 109:353–368
23. Tijssens MGA, Van Der Giessen E, Sluys LJ (2000) Simulation of mode I crack growth in polymers by crazing. Int J Solids Struct 37:7307–7327
24. Estevez R, Tijssens MGA, Van Der Giessen E (2000) Modeling of the competition between shear yielding and crazing in glassy polymers. J Mech Phys Solids 48:2585–2617
25. Seelig T (2008) Computational modeling of deformation mechanisms and failure in thermoplastic multilayer composites. Compos Sci Technol 68:1198–1208
26. Nielsen KL, Hutchinson JW (2012) Cohesive traction-separation laws for tearing of ductile metal plates. Int J Impact Eng 48:15–23
27. Whitney JM, Browning CE, Hoogsteden W (1982) A double cantilever beam test for characterizing mode I delamination of composite materials. J Reinf Plast Compos 1(4):297–313
28. Martin RH, Davidson BD (1999) Mode II fracture toughness evaluation using four point bend, end notched flexure test. Plast Rubber Compos 28(8):401–406
29. Benzeggagh ML, Kenane M (1996) Measurement of mixed-mode delamination fracture toughness of unidirectional glass/epoxy composites with mixed-mode bending apparatus. Compos Sci Technol 56(4):439–449
30. Alfano G, Crisfield MA (2001) Finite element interface models for the delamination analysis of laminated composites: Mechanical and computational issues. Int J Numer Methods Eng 50:1701–1736
31. Turon A et al (2007) An engineering solution for mesh size effects in the simulation of delamination using cohesive zone models. Eng Fract Mech 74(10):1665–1682
32. Mitsubishi chemical and carbon fiber composites (2017) Selector guide, Mitsubishi chemical carbon fiber and composites, Inc. Retrieved from http://mccfc.com/
33. Geleta TN, Woo K, Lee B (2017) Prediction of effective material properties for triaxially braided textile composite. Int J Aeronaut Sp Sci 18(2):222–235
34. Gibson RF (2015) Principles of composite material mechanics, 4th edn. CRC Press, Boca Raton
35. Christos C (1983) Chamis, simplified composite micromechanics equations for hygral, thermal and mechanics properties. Cleveland, Ohio
36. GENOA technical manual (2013)
37. ASTM D5528-94a (2001) Standard test method for mode I interlaminar fracture toughness of unidirectional fiber-reinforced polymer matrix composites. ASTM International, West Conshohocken, PA. www.astm.org
38. ASTM D7905/D7905M-14 (2014) Standard test method for determination of the mode II interlaminar fracture toughness of unidirectional fiber-reinforced polymer matrix composites. ASTM International, West Conshohocken, PA. https://doi.org/10.1520/D7905_D7905M-14
39. Moës N, Belytschko T (2002) Extended finite element method for cohesive crack growth. Eng Fract Mech 69(7):813–833
40. Dávila CG, Camanho PP, De Moura MF (2001) Mixed-mode decohesion elements for analyses of progressive delamination. In 42nd AIAA/ASME/ASCE/AHS/ASC Struct. Dyn. Mater. Conf. AIAA-02-1496, Seattle, Washington